DOI: 10.1002/cnma.201900561



## Carbon Nano-Onion and Zinc Oxide Composites as an Electron Transport Layer in Inverted Organic Solar Cells

Diana M. Bobrowska, [a] Edison Castro, [b] Luis Echegoyen, [b] and Marta E. Plonska-Brzezinska\*[c]

**Abstract:** We report a facile chemical method to synthesize hybrid nanocomposites containing carbon nano-onions (CNOs) and zinc oxide or hydroxide. The structure, surface morphology, optical properties and surface area of the CNOs were characterized by X-ray diffraction, scanning electron microscopy with energy dispersive spectroscopy, transmission electron microscopy, thermogravimetric analysis, infrared and Raman spectroscopies, and adsorption/desorption  $N_2$ 

techniques. For the first time, we demonstrate the fabrication of bulk heterojunction organic solar cell devices utilizing hybrid nanocomposites containing CNOs and ZnO as the electron transport layer. This configuration showed good photovoltaic performance with maximum external quantum efficiencies of 16.5 and 48.9% and power conversion efficiencies of 0.42 and 1.49% for the pristine ZnO and CNO/ZnO ( $m_{\text{CNO}}$ : $m_{\text{ZnO}}$ =1:4) layers, respectively.

### Introduction

Organic solar cells (OSCs) have attracted attention as a promising renewable energy source due to their attractive properties, such as low weight, low fabrication cost, large-scale production capability and flexibility.<sup>[1]</sup> In traditional OSCs, poly (3,4-ethylenedioxythiophene):polystyrene sulfonate (PEDOT: PSS) is used as a hole transport layer. Unfortunately, its acidic nature causes corrosion of the indium tin oxide (ITO) electrode and contributes to the degradation of the OSC device. Furthermore, since low-work-function metals such as Al are used as a top electrode they are easily oxidized and are sensitive to oxygen and water vapor.[2] To improve ambient device stability, an inverted OSC is frequently constructed that avoids the acidic nature of PEDOT:PSS and the sensitivity of Al. [3] In this configuration, high work function metals, such as Ag or Au, are used, which are more stable than Al. An electron transport layer (ETL) is located between the ITO and an active layer, which usually consists of an n-type inorganic metal oxide (such as ZnO, MoO<sub>x</sub> or TiO<sub>2</sub>).<sup>[4]</sup> The chemical strategies were also used to balanced photovoltaic parameters of the devices. [5.6] Increasing of molecular crystallinity of donor and acceptor materials may result in power conversion efficiency of over 16%.[8]

[a] Dr. D. M. Bobrowska Faculty of Chemistry University of Bialystok Ciolkowskiego 1 K, 15-245 Bialystok (Poland)

[b] Dr. E. Castro, Prof. L. Echegoyen Department of Chemistry University of Texas at El Paso, 500 W. University Ave., El Paso, TX 79968 (USA)

[c] Dr. M. E. Plonska-Brzezinska Department of Organic Chemistry Faculty of Pharmacy with the Division of Laboratory Medicine Medical University of Bialystok Mickiewicza 2 A, 15-222 Bialystok (Poland) E-mail: marta.plonska-brzezinska@umb.edu.pl In the present study, we used ZnO due to its interesting physico-chemical properties with a band gap of 3.37 eV, [9] which is not effective for visible light-driven photocatalysis. [10,11] ZnO is characterized by a high exciton binding energy (60 meV) and piezoelectricity at room temperature. [9,12] ZnO also has the advantages of low cost, easy preparation, high purity and crystallinity at low temperatures, [13] good transparency in the visible range, relatively high electron mobility and low toxicity. [14] As a result of these properties, it is widely used in photocatalysis, [15] solar cells, [16] lithium ion batteries, [11] gas sensors [17] or field-emission emitters.

Since the discovery of fullerenes by Kroto et al., carbon nanostructures (CNs) have attracted considerable attention. [19] They possess attractive properties that enable a broad range of applications in energy conversion, energy storage fields, sensors, biomedical diagnostics, lubrication, catalysis, gas storage, electromagnetic shielding, and optical limiting. [20–22] One of the allotropic forms of carbon is the carbon nano-onions (CNOs), also called multilayered fullerenes. "Small" CNOs consist of 6 to 8 curved graphene layers with increasing diameters and distances between them of ca. 0.334 nm. [23–25] "Small" spherical CNOs (average 5–6 nm diameter) are formed by thermal annealing of nanodiamond (ND) particles with diameters of ~5 nm. [26–28]

Pristine CNs and inorganic materials have many advantages, but their physico-chemical properties have some limitations. Certain limitations of these materials can be eliminated through the synthesis of composites. Composite materials based on the integration of CNs with other substances can lead to substances possessing the properties of the individual components. The preparation of composites containing CNOs and organic or inorganic components has been reported. [29,30,31,32,33] In this work, we prepared hybrid nanocomposites containing CNOs and inorganic materials, namely zinc oxide or hydroxide.

To date, many synthetic methods, such as laser ablation,<sup>[34]</sup> hydrothermal synthesis,<sup>[35,36]</sup> vapor transport processes,<sup>[37]</sup> electrochemical deposition, and sol-gel methods,<sup>[38,39]</sup> have been used to produce metal hydroxides/oxides with various shapes,

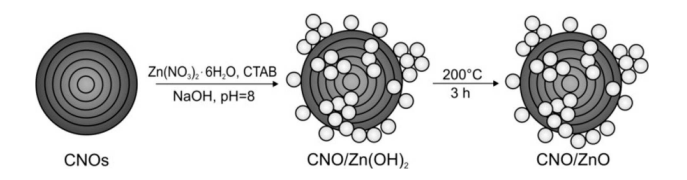
sizes and structures. We developed a one-step and highly-efficient precipitation synthesis method of precursors and hybrid materials containing CNOs and zinc components that is easy, environmentally friendly and economical and is morphology- and structure-sensitive.<sup>[15]</sup> First, we formed Zn(OH)<sub>2</sub> and then thermally transformed it into ZnO.<sup>[40,41]</sup> In the presence of surfactants, we used ZnO to modify the CNO surfaces and then applied these composites as electron transporting layers (ETL) in inverted OSCs.

#### **Results and Discussion**

# Preparation and Characterization of Composites Containing CNOs and Zn(OH), or ZnO

The Zn(OH)2, ZnO and their composites were synthesized by a widely used precipitation! method, which is schematically shown in Scheme 1. Changing one of the synthetic conditions, such as additives, pH, temperature or reagent, causes a significant modifications of the morphology and physicochemical properties of the resulting zinc materials. However, Zn (OH)<sub>2</sub> and ZnO are thermodynamically stable over a pH range of 7–14 at 0.01 M Zn<sup>2+</sup> concentration. Their formation has been observed at lower pH, namely Zn(OH), at ca. 6 pH and ZnO at 9 pH.[42] During the synthesis of Zn(OH)2, NaOH was added dropwise to achieve a pH equal to 8 to obtain the solid form of Zn(OH)<sub>2</sub> (Eq. 1 and 2). In aqueous solution at a pH higher than 9, Zn(II) exists as hydroxyl complexes, such as Zn(OH)<sub>4</sub><sup>2-</sup> (Eq. 3). [43] The general reaction of the formation of Zn(OH), by precipitation and heat treatment can be represented as (Eq. 1, 2 and 4):[15]

$$Zn(NO_3)_2 (aq) \xrightarrow{NaOH} Zn(OH)_2 (amorph.) \xrightarrow{30-60^{\circ}C} \varepsilon - Zn(OH)_2$$
 (1)



Scheme 1. Schematic representation of the synthesis of  $\text{CNO/Zn}(\text{OH})_2$  and CNO/ZnO composites.

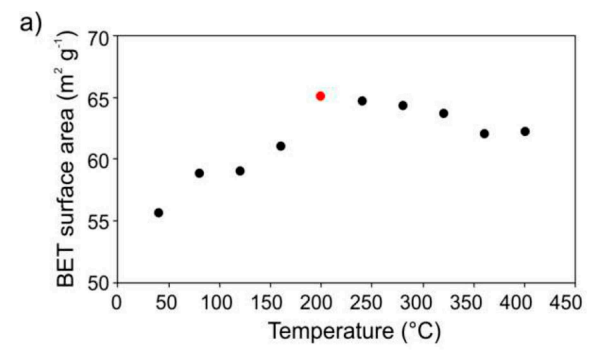
$$Zn^{2+} + 2OH^- \rightarrow Zn(OH)_2(s)$$
 (2)

$$Zn(OH)_2(s) + 2OH^- \rightleftharpoons Zn(OH)_4^{2-}$$
(3)

$$Zn(OH)_2 \xrightarrow{>60^{\circ}C} ZnO$$
 (4)

Thermal decomposition of  $Zn(OH)_2$  and simultaneous formation of ZnO occurs at temperatures between 70 and  $140\,^{\circ}C.^{[44]}$  This process depends on the type of  $Zn(OH)_2$  crystal structure.  $Zn(OH)_2$  was tested by the  $N_2$  adsorption method to select the optimal parameters (temperature and time of calcination) for the formation of ZnO with the highest surface area (S). S was calculated using the Brunauer-Emmett-Teller theory ( $S_{BET}$ ). Based on the BET study (Figure 1), the calcination of  $Zn(OH)_2$  was performed at  $200\,^{\circ}C$  for 3 h.

To study the stability and estimate the mass ratio of the inorganic component to CNOs in the composites, thermogravimetric analysis was performed (Figure 2 and Table 1). The onset of oxidation, inflection and end temperatures, and total weight loss results are summarized in Table 1, which correspond to the



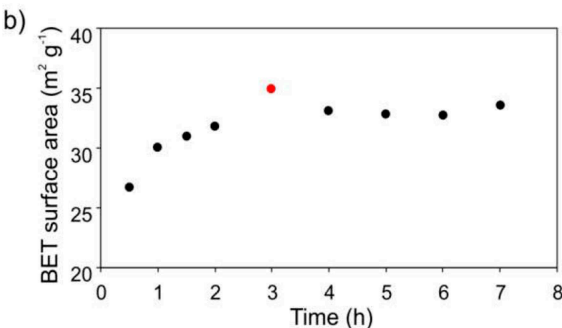
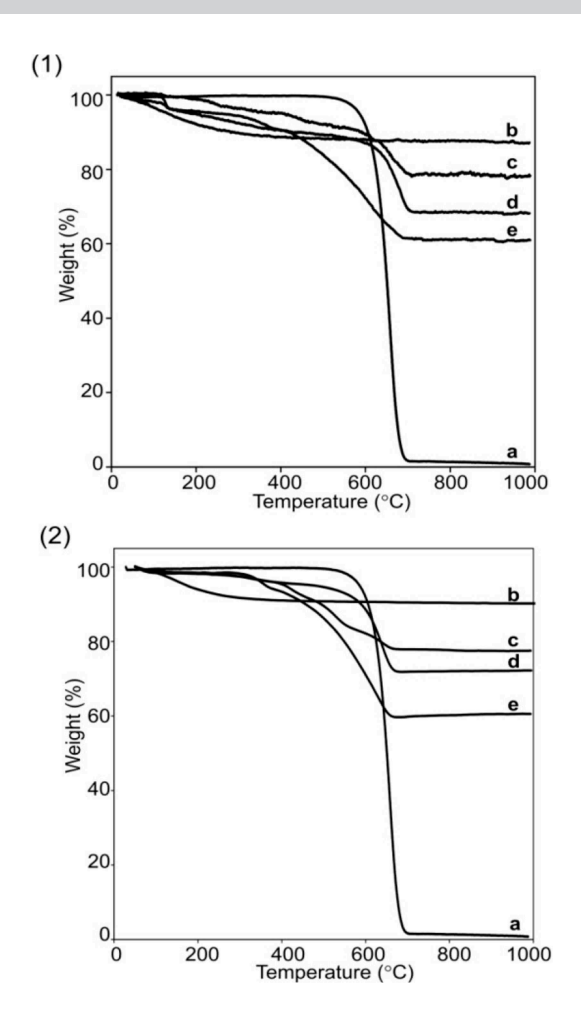


Figure 1. The S<sub>BET</sub> of Zn(OH)<sub>2</sub> calculated vs. (a) temperature and (b) time.

Sample	Onset temperature [°C]	Inflection temperature [°C]	End temperature [°C]	Total weight loss [%]		
CNO	600	650	700	98		
Zn (OH) <sub>2</sub>	30	140	250	15		
CNO/Zn (OH) <sub>2</sub> (1:4)	610	680	700	20		
CNO/Zn (OH) <sub>2</sub> (1:3)	600	685	700	33		
CNO/Zn (OH) <sub>2</sub> (1:1.5)	450	600	690	40		
ZnO	30	-	-	2		
CNO/ZnO (1:4)	420	630	682	20		
CNO/ZnO (1:3)	600	640	680	35		
CNO/ZnO (1:1.5)	315	630	675	41		



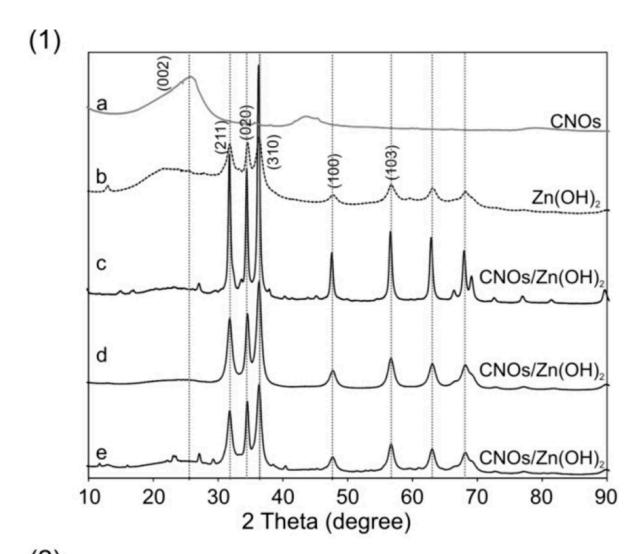
**Figure 2.** TGA weight loss curves for (a) CNOs, (b) the pristine inorganic component, and CNO composites with  $Zn(OH)_2$  (panel 1) or ZnO (panel 2) with different mass ratios of (c) 4:1, (d) 3:1, and (e) 1.5:1.

initial weight loss, maximum weight loss and final weight from the TGA graphs, respectively. The onset temperature, inflection temperature and end temperature for all composites containing CNOs and zinc components are associated with the combustion of carbon material. In the temperature range between 50 and 1000 °C, Zn(OH)<sub>2</sub> and ZnO are stable. In Figure 2a, the TGA curve of the CNOs shows complete thermal decomposition over 700 °C. One sharp transition in the CNO sample signifies that the material is a homogeneous single phase with no impurities. The TGA curve of Zn(OH)<sub>2</sub> shows a mass loss over 120 °C (Figure 2b, panel 1), which is attributed to removal of the moisture or surface hydroxyl groups.

Furthermore, there is evidence of the successful transformation of  $\rm Zn(OH)_2$  to  $\rm ZnO$  that is stable in the temperature range of up to  $1000\,^{\circ}\rm C$  (Figure 2b, panel 2). The final temperature of the decomposition is related to the combustion of carbonaceous materials. Based on the weight loss in the composites, the mass ratios of the inorganic component to the carbon material were calculated and are summarized in Table 1. The values of total weight loss were approximately 20, 35 and 40%, which corresponded to mass ratios of the CNOs to the zinc components of ca. 1:4; 1:3 and 1:1.5, respectively.

The XRD patterns of the powder materials are shown in Figure 3. An asymmetric broad reflection is present in the range between 23 and 27° and there is a maximum asymmetric broad reflection at ca.  $2\theta = 25.30^{\circ}$  (d = 3.454 Å). This peak is related to the reflection of the X-rays from the (002) plane and can be assigned to two separate forms of carbon, namely turbostratic carbon (amorphous) and graphene carbon (graphitic carbon). The peak at a  $2\theta$  at ca. 43.67° (d=2.085 Å) corresponds to the (111) basal plane diffraction of the diamond structure (JCPDS No. 75-1621). The diffraction peaks, which are shown in Figure 3a, panel (1), can be indexed to wulfingite Zn(OH)<sub>2</sub> (JCPDS No. 38-0385). [40]

The XRD pattern for ZnO shows several reflections at ca.  $2\theta$  = 31.85, 34.51, 36.23, 47.44, 56.52, 62.76, 66.32, 67.91 and 68.83. These signals are related to the reflection of the X-rays from the (100), (002), (101), (102), (110), (103), (200), (112) and (201) planes, respectively, and can be assigned to the hexagonal ZnO wurtzite phase (JPCDS No. 36–1451). [48.49] This



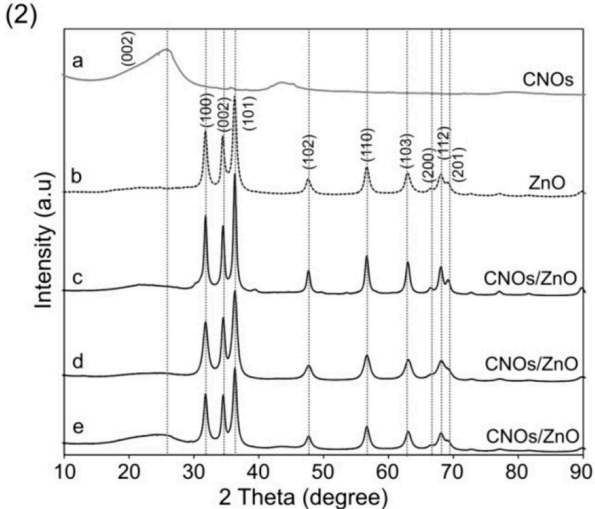


**Figure 3.** XRD patterns of zinc hydroxide (panel 1) and zinc oxide (panel 2) with their composites: (a) CNOs, (b) pristine inorganic component, and CNO/Zn(OH) $_2$  or CNO/ZnO with different mass ratios (c) 1:4, (d) 1:3 and (e) 1:1.5.





ZnO phase is one of the most stable forms.<sup>[17]</sup> The XRD patterns of composites containing CNOs consist of reflections from both the inorganic and carbon components. The reflections from the CNO planes are very low in intensity because of the small amount of carbon materials in the composites. No other impurities or additional peaks were observed, which confirmed the high purity of the synthesized products.

It has been reported previously that flower-like crystallites of zinc materials are a consequence of the usage of zinc nitrate

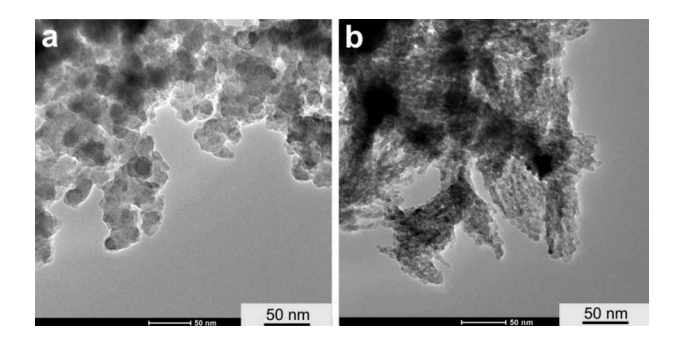


Figure 4. HRTEM images of (a) ZnO and (b) CNO/ZnO (1:4).

as a precursor<sup>[50,51]</sup> or the rapid addition of sodium hydroxide into a vigorous stirred solution.<sup>[50]</sup> Figures 4f and 4 g show high-resolution transmission electron microscopy (HRTEM) images of zinc oxide and CNO/ZnO composite in a mass ratio of 1:4. After calcination, the sample shows very regular and granular structures with diameters of approximately 10–15 nm (Figure 4g).

The surface morphologies of pristine Zn(OH)<sub>2</sub>, ZnO and their composites, which were obtained with different mass ratios, were studied using scanning electron microscopy (SEM). Figure 4a shows uncoated CNOs that are not firmly homogenous. Furthermore, it was observed that Zn(OH)<sub>2</sub> formed aggregates. The ZnO structure is more granular and uniform after calcination at 200 °C (Figure 4b and 4c). Images in Figure 4d and 4e show that composites containing CNOs and ZnO or Zn(OH)<sub>2</sub> present a similar morphology and formed flower-like crystallites. The shape of the crystallites depends on different factors, such as pH, zinc source or the presence of additional substances.

The energy-dispersive X-ray (EDX) spectra confirmed the presence of Zn and O in the CNO composites (Figure 4h and 4i). Figures 5h–5j, panel 1, illustrate the distribution profiles for

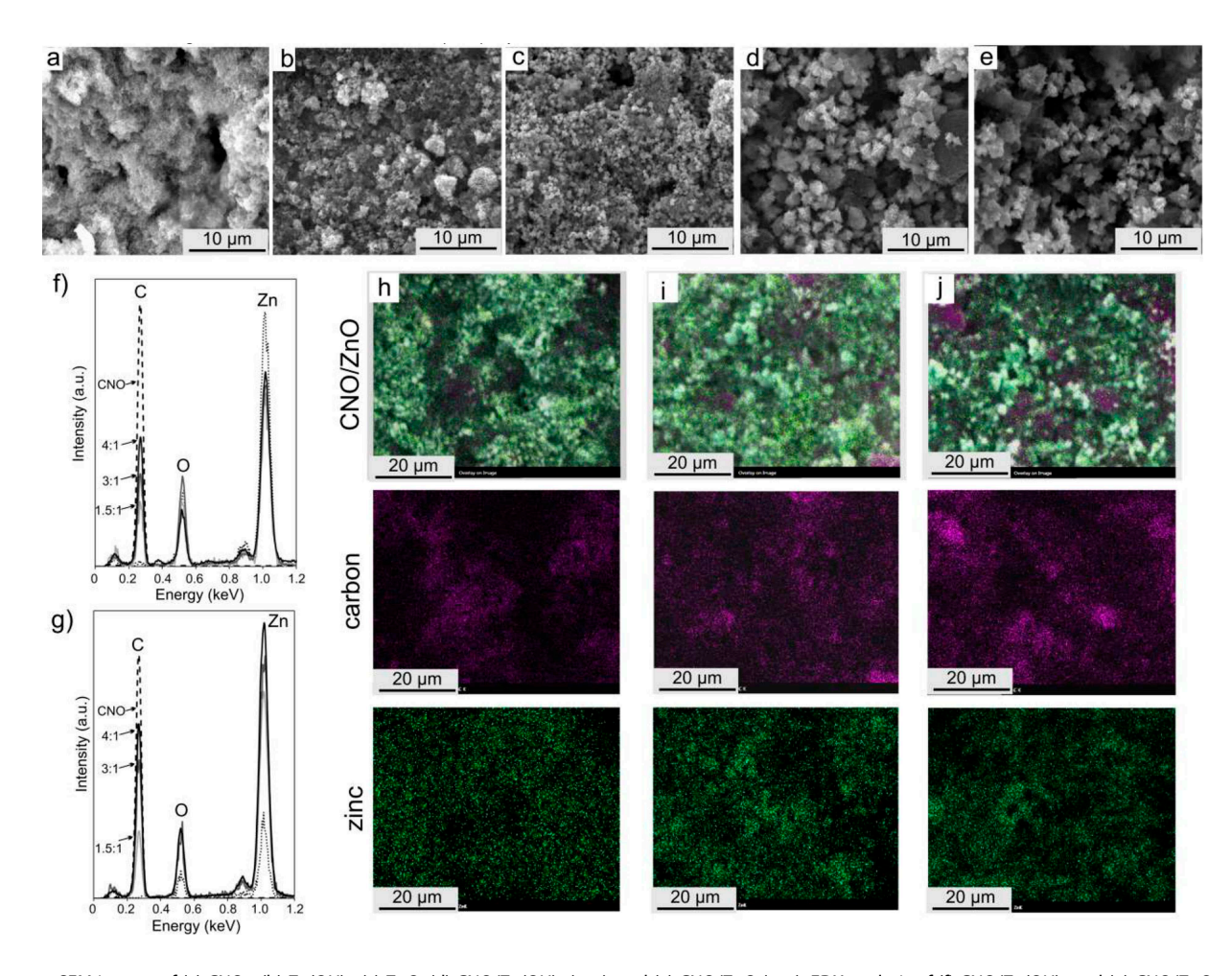


Figure 5. SEM images of (a) CNOs, (b) Zn(OH)<sub>2</sub>, (c) ZnO, (d) CNO/Zn(OH)<sub>2</sub> (1:4), and (e) CNO/ZnO (1:4). EDX analysis of (f) CNO/Zn(OH)<sub>2</sub> and (g) CNO/ZnO composites with different mass ratios. Mapping by EDX technique for (h) CNO/ZnO (1:4), (i) CNOs/ZnO (1:3), (j) CNOs/ZnO (1:1.5). Overlay is distribution of elements on SEM images in hybrid composites: carbon (purple), zinc (dark green) and oxygen (light intense green).





carbon, zinc and oxygen in the composites, which were obtained with different mass ratios, which were studied using mapping of EDX. The results indicate the presence and a uniform distribution of three elements in the composites and show the presence of CNO and ZnO across the entire experimental area.

Atomic Force Microscopy (AFM) is a useful tool to monitor the topography of the surface and to study interactions between the AFM tip and the sample. The tapping mode AFM images of ZnO and CNO/ZnO (1:4) are shown in Figure 6. Topographic cross section analysis of both layers

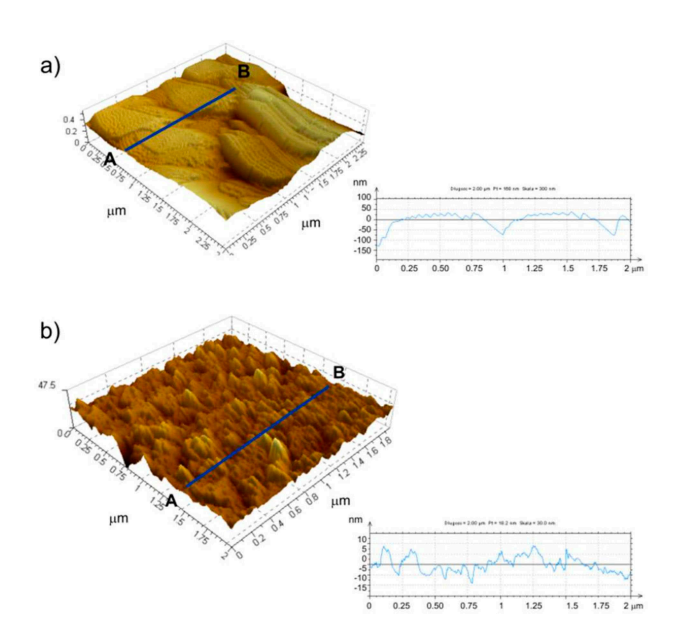


Figure 6. Tapping mode AFM images of (a) ZnO and (b) CNOs/ZnO (1:4); corresponding topographic cross section analyses of AFM images along the AB directions are presented in each image.

along the AB direction are also presented in Figure 6. ZnO formed terrace structures with a height of ca. 100 nm (Figure 6a). The distance between two neighbouring terrace structures is ca. 1  $\mu$ m. The AFM image of CNO/ZnO immobilized surface is shown in Figure 6b. The film shows higher homogeneity and roughness (Figure 6b, cross-section analysis along AB direction) in comparison to pristine ZnO. Topographic cross-section analysis along this direction shows that this film has a height of ca. 15 nm.

The Raman spectra confirmed the presence of CNOs and inorganic components in the composites (Figure 7). All characteristic Raman modes for the Zn(OH)2, ZnO and carbon composites, such as  $E_2^{high}$ ,  $E_2^{low}$ ,  $E_2^{high}$ ,  $A_1^{low}$ , D, G and 2D, are summarized in Table 2. The CNO spectrum (Figure 7a) shows two main bands, namely G and D, that are characteristic of carbon nanostructures. The G band at ca. 1582 cm<sup>-1</sup> is associated with the  $E_{2q}$  phonon mode of  $sp^2$ -hybridized carbon atoms, and the D band at ca. 1339 cm $^{-1}$  is associated with the breathing mode of k-point phonons with  $A_{1g}$  symmetry. [52-54] The E<sub>2</sub><sup>high</sup> mode is characteristic of the wurtzite phase of ZnO.<sup>[55]</sup> The E<sub>2</sub> mode consists of two modes of low- and high-frequency phonons (E<sub>2</sub><sup>low</sup>, E<sub>2</sub><sup>high</sup>), which correspond to the vibration of the heavy zinc sublattice and oxygen atoms, respectively.<sup>[56]</sup> The peak positioned ca. 1120 cm<sup>-1</sup> in all Raman spectra is likely related to the glass substrate<sup>[57]</sup> or to the acoustic combination of multiphonons  $A_1$  and  $E_2$ . [56,58] The D band located at 1339 cm<sup>-1</sup> for pristine CNOs is shifted to higher frequencies for the composites, from 1341 to 1348 cm<sup>-1</sup>. Additionally, the highly dispersive second-order harmonic of the 2D band (2678 cm<sup>-1</sup> for pristine CNOs) is shifted to higher frequencies, up to 2695 cm<sup>-1</sup> for  $CNOs/Zn(OH)_2$  (1:4).

The presence of CNOs and zinc components in the composites was confirmed using Fourier transform infrared (FTIR) spectroscopy. The FTIR spectra of the CNOs, Zn(OH)<sub>2</sub>, ZnO and their composites are shown in Figure 8. The CNO infrared

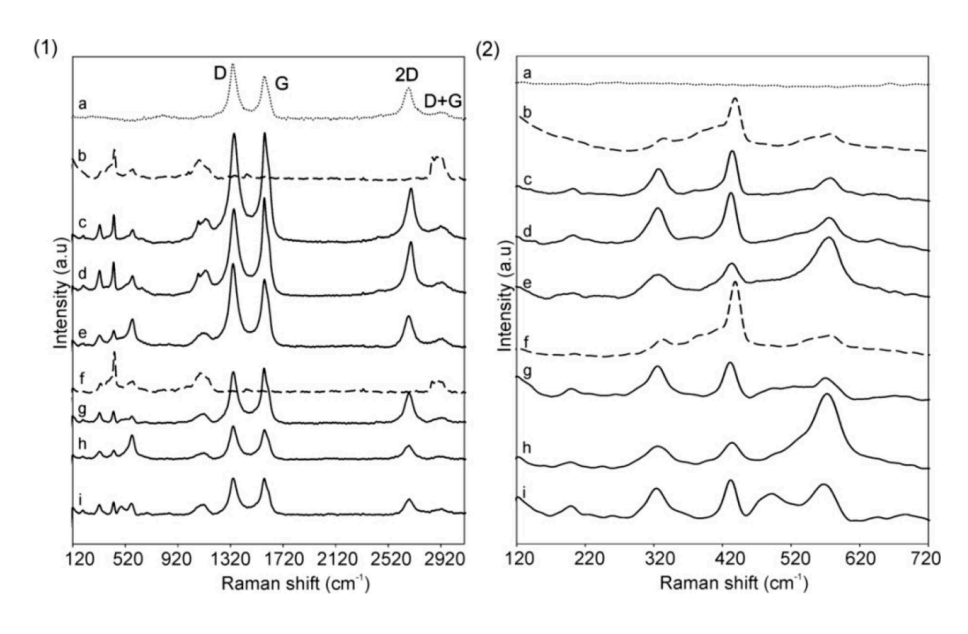


Figure 7. Raman spectra of (a) CNOs, (b) Zn(OH)<sub>2</sub>, (c) CNO/Zn(OH)<sub>2</sub> (1:4), (d) CNO/Zn(OH)<sub>2</sub> (1:3), (e) CNO/Zn(OH)<sub>2</sub> (1:1.5), (f) ZnO, (g) CNO/ZnO (1:4), (h) CNO/ZnO (1:3), and (i) CNO/ZnO (1:1.5) from 120 to 3200 cm<sup>-1</sup> (panel 1) and from 120 to 720 cm<sup>-1</sup> (panel 2).



Table 2. Raman-active phonon-mode frequencies for CNO/Zn(OH) <sub>2</sub> and CNO/ZnO materials and their pristine components.						
Sample	Mode [cm $^{-1}$ ] $E_2^{\text{high}} - E_2^{\text{low}}$	E <sub>2</sub> high	$A_1^{low}$	D	G	2D
CNO	-	-	-	1339	1579	2678
Zn(OH) <sub>2</sub>	335	438	577	_	_	-
CNO/Zn(OH) <sub>2</sub> (1:4)	327	434	577	1348	1582	2695
CNO/Zn(OH) <sub>2</sub> (1:3)	326	432	575	1347	1579	2693
CNO/Zn(OH) <sub>2</sub> (1:1.5)	327	434	575	1342	1580	2679
ZnO	333	439	577	-	-	-
CNO/ZnO (1:4)	326	431	570	1343	1577	2679
CNO/ZnO (1:3)	325	434	572	1342	1579	2680
CNO/ZnO (1:1.5)	324	432	567	1341	1578	2680

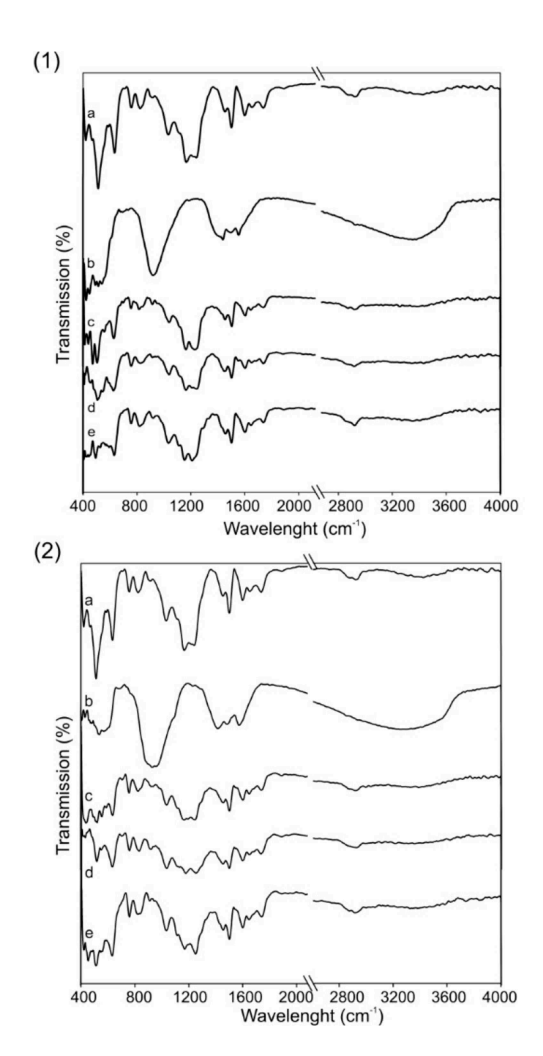


Figure 8. Infrared spectra of zinc hydroxide (panel 1) and zinc oxide (panel 2) with their composites: (a) CNOs, (b) inorganic materials, CNO/Zn(OH)<sub>2</sub> or CNO/ZnO with different mass ratios (c) 1:4, (d) 1:3 and (e) 1:1.5.

spectrum shows a peak at 1599 cm<sup>-1</sup> corresponding to aromatic C=C stretching vibration, which confirmed the presence of *sp*<sup>2</sup>-hybridized carbon atoms in the CNs.<sup>[59]</sup> Two bands occurring at 1247 and 1741 cm<sup>-1</sup> can be assigned to C=O=C and C=O stretching vibrations, respectively.<sup>[60]</sup> The presence of oxygen in the carbon sample is probably caused by the annealing of the CNOs after their formation at 400 °C in air. The characteristic

signal at  $1178\,\mathrm{cm^{-1}}$  is assigned to the innermost shell of the CNOs.  $^{[61]}$ 

The stretching mode of the ZnO appears at 927 cm<sup>-1</sup> due to the metal oxide bond. [62] The absorption band at 480 cm<sup>-1</sup> is assigned to the stretching vibration of the Zn–O lattice. [10] The band observed at 927 cm<sup>-1</sup> results from asymmetric stretching vibrations of Zn-O–Zn bridge oxygens in the structure. [42] Two bands observed at ca. 3020 and 995 cm<sup>-1</sup> can be assigned to =C–H and =CH2 stretching vibrations in CNOs. [27] Additionally, the two bands occurring at 1741 and 1245 cm<sup>-1</sup> can be assigned to C=O bonds, which likely result from the additional annealing of the CNOs at 400 °C in air. [26]

The porosity, pore-size distribution, and specific surface areas of the CNOs, zinc materials and their composites were determined by the  $N_2$  adsorption/desorption technique (Table 3). The BET specific surface area ( $S_{BET}$ ) values of all samples are summarized in Table 3.

The  $S_{BET}$  measured for hybrid materials is in the range of 84–178 m<sup>2</sup>g<sup>-1</sup>, where the largest values were determined for samples with the highest content of CNOs. The  $Zn(OH)_2$  has an  $S_{BET}$  value that is two times higher than that obtained for ZnO. Based on their pore size and their porous properties, the inorganic materials have macroporous morphologies and the pores between the crystallites have a diameter greater than 50 nm. The CNOs have more mesoporous characteristics with diameters of 2–50 nm.

### Photovoltaic Properties of CNO and ZnO Composites

We prepared inverted organic solar cells with composites of CNOs and zinc oxide as the electron transporting layers (ETLs). The ETL and active layer in the devices were made by the spin-coating technique. As the active layer, a standard mixture of [6,6]-phenyl-C61-butyric acid methyl ester (PCBM) and poly(3-hexylthiophene-2,5-diyl) (P3HT) was used, which form a bulk heterojunction system. As a metal electrode, Ag was used as an efficient hole-collecting electrode. [63]

The external quantum efficiency (EQE) was also measured, and the spectra of the devices using ZnO and CNO/ZnO as the ETL are shown in Figure 9a. A broad optical absorption was observed between 300 and 650 nm.

The ITO/ZnO/P3HT:PCBM/Ag device showed a maximum EQE of 16.5% at 500 nm, with a clear contribution to the

Table 3. The porosity of the CNO/ZnO and the CNO/Zn(OH) $_2$ composites and of their reference compounds based on N $_2$ adsorption/desorption isotherms.					
Sample	$S_{BET}^{[a]}$ $[m^2g^{-1}]$	$S_{\rm ext}^{[b]}$ [m <sup>2</sup> g <sup>-1</sup> ]	Pore volume [cm³ g <sup>-1</sup> ]	Average pore size [nm]	
CNO	453	_	1.44 <sup>[c]</sup>	13.9	
Zn(OH) <sub>2</sub>	74	59	0.35 <sup>[d]</sup>	80.7	
CNO/Zn(OH) <sub>2</sub> (1:4)	84	56	0.24 <sup>[e]</sup>	71.2	
CNO/Zn(OH) <sub>2</sub> (1:3)	95	63	0.44 <sup>[f]</sup>	63.4	
CNO/Zn(OH) <sub>2</sub> (1:1.5)	104	65	0.67 <sup>[g]</sup>	57.8	
ZnO	33	33	0.18 <sup>[h]</sup>	182.9	
CNO/ZnO (1:4)	98	121	0.69 <sup>[i]</sup>	33.8	
CNO/ZnO (1:3)	143	111	0.58 <sup>[j]</sup>	42.0	
CNO/ZnO (1:1.5)	178	82	0.48 <sup>[k]</sup>	60.9	

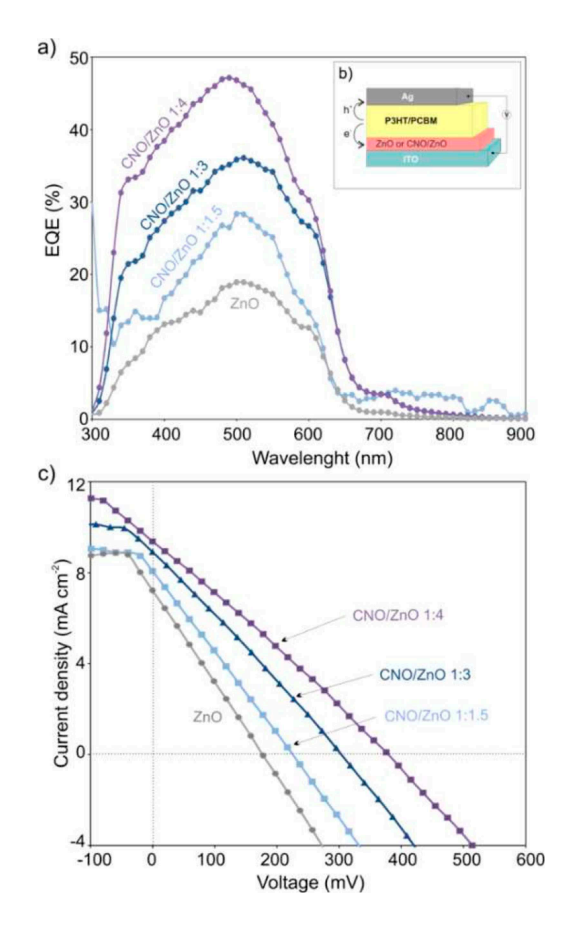


**Figure 9.** (a) EQE spectra and (c) I–V characteristics of devices containing (b) CNO/ZnO and ZnO as ETLs.

photocurrent from the active layer and ZnO.<sup>[64]</sup> In the EQE spectrum, the peak at ca. 350 nm results from the absorption of ZnO.<sup>[64]</sup> The maximum EQE increased from 16.5 to 48.9% for devices containing ZnO and CNO/ZnO (1:4) layers, respectively. The EQE values increased with the content of ZnO in the ETL, and the maximum value (48.9%) was obtained for CNO/ZnO (1:4) in the ETL.

The current density-voltage (I–V) characteristics of the spectral response with the solar spectrum (AM1.5G illumination,

100 mW cm<sup>-2</sup>) are shown in Figure 9c, and the parameters of the corresponding devices, such as open-circuit voltage  $(V_{\alpha c})$ , short-circuit current density (I<sub>sc</sub>), fill factor (FF) and power conversion efficiency (PCE), are summarized in Table 4. The inverted OSC device with CNO/ZnO (1:4) exhibited the best photovoltaic parameters (Table 4). The highest PCE (1.49%) was obtained for a device with CNO/ZnO (1:4) as the ETL. Compared to the reference device with pristine ZnO, the photovoltaic parameters are lower (PCE of 0.42%,  $V_{\rm OC}$  of 0.188 V,  $I_{\rm SC}$  of 7.22 mA cm<sup>-2</sup>, and FF of 0.31) than those for devices containing the CNO/ZnO composites as the ETL. The work function of ZnO and CNO/ZnO (1:4) were obtained at 4.89 eV and 4.38 eV, respectively. For comparison, the ionization potential of pristine onion-like carbons was determined as 5.23 eV and the value of optical bandgap for thin films containing onion-like carbons was deduced as 2.02 eV.[65]

The values of  $I_{SC}$  for all samples are between 7 and 9 mA cm<sup>-2</sup>. The FF values for the ZnO and CNO/ZnO (1:4) devices are 0.31 and 0.41, respectively. An increase in the OSC parameters for devices containing CNO/ZnO composites was observed. Additionally, the highest values of the device parameters were observed for the devices with a high content of ZnO.

#### Conclusion

In conclusion, a facile one-step precipitation synthesis of the CNO and zinc hydroxide/oxide composites was developed. ε-Zn (OH)<sub>2</sub> and ZnO in the presence of CTAB and their composites, including CNOs, were successfully obtained. The ZnO-based hybrid composites show photoactive properties that were

Table 4. Summary of OSC device parameters.						
Sample	$\rm I_{sc}~[mAcm^{-2}]$	$V_{oc}[V]$	FF [—]	PCE [%]		
ZnO CNO/ZnO (1:4) CNO/ZnO (1:3) CNO/ZnO (1:1.5)	7.22 9.37 8.91 8.06	0.188 0.389 0.302 0.253	0.31 0.41 0.38 0.36	0.42 1.49 1.02 0.73		





confirmed using current-density-voltage characteristics and external quantum efficiency measurements. This study is the first to use CNO/ZnO with different mass ratios of both components as the electron transport layer in inverted OSCs. A power conversion efficiency of 0.42 and 1.49% and an external quantum efficiency as high as 16.5 and 48.9% were observed for the pristine ZnO and CNO/ZnO ( $m_{\text{CNO}}$ : $m_{\text{ZnO}}$ =1:4), respectively.

## **Experimental Section**

#### Reagents and Materials

Unless noted, all chemicals and solvents were commercially available and used as received without further purification. We used zinc(II) nitrate hexahydrate (>97.0%, Sigma-Aldrich, Poland), ethanol (99.8%, Avantor Performance Materials Poland S.A.), hexadecyltrimethylammonium bromide (CTAB,  $\geq$ 98%, Sigma-Aldrich, Poland), sodium hydroxide (Avantor Performance Materials Poland S.A.), o-dichlorobenzene (o-DCB, Sigma-Aldrich, Poland), regioregular poly(3-hexylthiophene-2,5-diyl) (P3HT, Sigma-Aldrich, Poland), [6,6]-phenyl-C61-butyric acid methyl ester (PCBM, >99%, Sigma-Aldrich, Poland) and nanodiamond (ND) powder (Carbodeon  $\mu$ Diamond\* Molto, Vantaa, Finland) with a crystal size between 4 and 6 nm and ND content  $\geq$ 97 wt.%. All aqueous solutions were made using deionized water, which was further purified with a Milli-Q system (Millipore). All starting reagents were used without further purification.

#### **Instruments and Measurements**

The materials were imaged by secondary electron scanning electron microscopy (SEM) using an FEI Tecnai S-3000 N (Tokyo, Japan). The accelerating voltage of the electron beam was 20 keV. The energy dispersive X-ray (EDX) spectroscopy analyses were performed with the ASPEX System, fully integrated and automated with the SEM. The high-resolution transmission electron microscopy (TEM) images were recorded using the FEI Tecnai Instrument. The TEM point resolution was 0.25 nm, the TEM line resolution was 0.144 nm, and the accelerating voltage of the electron beam was 200 keV. Thermogravimetric analyses were performed using an SDT 2960 simultaneous TGA-DTG (TA Instruments). The heating rate was 10°C min<sup>-1</sup> in an air atmosphere (100 mLmin<sup>-1</sup>). X-ray diffraction data of powder samples were collected at 293 K using a SuperNova diffractometer (Agilent) with a CCD detector and a Cu–K $\!\alpha$  radiation at a 150 mm sample-to-detector distance. All samples for crystallography experiments were loaded into capillaries with a diameter of 0.5 mm. The N<sub>2</sub> gas adsorption measurements were performed using a Micromeritics apparatus (ASAP2020 automatic sorption analyser, Micromeritics Corp., USA) at −196 °C. Prior to gas adsorption analysis, the samples containing ZnO were degassed at 200 °C and at 35 °C for samples with Zn(OH)2 under low vacuum (10 μm Hg) for 12 h to remove any adsorbed species. The room-temperature Raman spectra recorded using a Renishaw spectrometer. An Ar + laser with a wavelength of 514 nm was employed as the excitation source. The positions of the Raman peaks were calibrated using a Si thin film as an external standard. The Raman spectra were registered at a spectral resolution of  $2\,\mathrm{cm}^{-1}$  and wavelengths between 100 and 3200  $\mathrm{cm}^{-1}$ . The Fourier Transform Infrared (FTIR) spectra were recorded in the range between 400 and 4000 cm<sup>-1</sup> at a resolution of 4 cm<sup>-1</sup> using a NICOLET IN10 MX Thermo Scientific spectrometer. Infrared spectra were recorded using an MCT detector cooled with liquid nitrogen to increase the sensitivity of the measurements. Additionally, an atmospheric correction was applied. Quantum efficiencie were determined using an IQE-2000 NEW-PORT quantum efficiency measurement system. The measurement was carried out at room temperature under illumination by monochromatic light from a xenon lamp (100 W). Spectra were registered at wavelengths between 350 and 1100 nm.

#### **Preparation of Carbon Nano-Onions**

Nanodiamonds (NDs), with a crystal size between 5 and 6 nm, were placed in a graphite crucible and transferred to an Astro carbonization furnace. Annealing of ultradispersed NDs was performed at 1650 °C under a 1.1 MPa He atmosphere with a heating ramp of 20 °Cmin<sup>-1</sup>. The final temperature was maintained for one hour, and then the material was slowly cooled to room temperature over a period of one hour. The furnace was opened, and the CNOs were annealed in air at 400 °C to remove any amorphous carbon.

#### Preparation of Zn(OH), and ZnO in the Presence of CTAB

The synthesis of Zn(OH)<sub>2</sub> was carried out using chemical precipitation.<sup>[51]</sup> The synthesis of pure materials and their composites was carried out in the presence of hexadecyltrimethvlammonium bromide (CTAB) as a surfactant to achieve better dispersion of the CNOs in water. CTAB was selected from a few surfactants, such as sodium dodecyl sulfate, sodium dodecyl benzene sulfonate, 4-(1,1,3,3-tetramethylbutyl)phenyl-polyethylene glycol and polyethylene glycol sorbitan monolaurate, because it exhibits the highest stability for CNO water dispersions. These results were published in a previous study. [67] The typical synthesis was initiated by the formation of Zn(OH)2, which was transformed to ZnO by heating. Initially, 100 mg zinc(II) nitrate hexahydrate was dissolved in 9 mL of a mixture of water and ethanol  $(m_{H2O}: m_{C2HSOH} = 1:1)$ . Then, 1 mL of 2.74 mM CTAB was added and stirred for 30 min. Subsequently, 0.1 M NaOH was added dropwise into a solution with vigorous stirring to establish a pH equal to 8. The Zn(OH)<sub>2</sub> white powder was collected and washed several times with ethanol until no alkaline pH was detected. Subsequently, Zn (OH), was dried for 24 h at 30 °C in an oven. Calcination of Zn(OH), at 200 °C for 3 h yielded ZnO.

## Preparation of the CNO/Zn(OH)<sub>2</sub> and CNO/ZnO Composites with Different Mass Ratios

To prepare CNO/Zn(OH)<sub>2</sub> nanocomposites with different mass ratios of both components, 10 mg of the CNOs was dispersed in 1 mL of anhydrous ethanol and sonicated. The suspension was then mixed with 1 mL of an aqueous solution of CTAB (2.74 mM) and stirred for 3 h. The different masses (80, 120, 150 mg) of zinc nitrate hexahydrate were then added to an aqueous dispersion of CNO/CTAB. Afterwards, 0.1 M sodium hydroxide solution was added until the pH reached 8 and the precipitation of the white powder was visible. The excess surfactant and unreacted reagents were removed by washing the powder several times with ethanol. CNO/Zn(OH)<sub>2</sub> composites with mass ratios of 1:4, 1:3 and 1:1.5 were obtained. The CNO/ZnO composites were obtained by calcination at 200 °C for 3 h.

#### **Device Fabrication**

An inverted OSC with the schematic configuration of ITO/(ZnO or CNO/ZnO)/P3HT:PCBM/Ag is shown in Figure 7b. All OSCs were





prepared in an ambient nitrogen atmosphere. Before preparation of the OSCs, all dispersions or solutions (e.g., ZnO, CNO/ZnO, P3HT, PCBM) were mixed and heated at 50 °C for 24 h on a hot plate. Prestructured ITO-coated glass was cleaned successively with deionized water with detergent, deionized water, acetone and isopropanol. Each solution/dispersion was ultrasonicated for 30 min. A volume of 150 µL of CNO/ZnO dispersion in ethanol (15 mg mL<sup>-1</sup>) was spin-coated at 2000 rpm for 30 s. After that, the electron transport layer (ETL) deposited on the ITO surface was annealed at 200 °C on the hot plate for 10 min. The active layer, which consisted of a mixture of P3HT and PCBM in a weight ratio of 1.25:1 in o-DCB, was spin-coated on the ETL at 2500 rpm for 60 s. Next, the devices were annealed in air at 110 °C for 15 min to completely evaporate the solvents. Finally, a sputtered 100 nm thick Ag top electrode film was deposited with a special cathode mask.

## **Acknowledgements**

We gratefully acknowledge the financial support of the National Science Centre, Poland (grant #2012/05/E/ST5/03800) to M.E.P.-B. L.E. thanks the Robert A. Welch Foundation for an endowed chair, grant #AH-0033 and the US NSF, grants: PREM programme (DMR-1205302) and CHE-1801317.

#### Conflict of Interest

The authors declare no conflict of interest.

**Keywords:** carbon nano-onions ⋅ composites ⋅ organic solar cells

- [1] Z. Xue, X. Liu, N. Zhang, H. Chen, X. Zheng, H. Wang, X. Guo, ACS Appl. Mater. Interfaces 2014, 6, 16403–16408.
- [2] R. Pacios, A. J. Chatten, K. Kawano, J. R. Durrant, D. D. C. Bradley, J. Nelson, Adv. Funct. Mater. 2006, 16, 2117–2126.
- [3] T. Stubhan, H. Oh, L. Pinna, J. Krantz, I. Litzov, C. J. Brabec, Org. Electron. 2011, 12, 1539–1543.
- [4] Y. He, T. Heumüller, W. Lai, G. Feng, A. Classen, X. Du, C. Liu, W. Li, N. Li, C. J. Brabec, Adv. Energy Mater. 2019, 9, 1900409.
- [5] J. Yuan, Y. Zhang, L. Zhou, G. Zhang, H.-L. Yip, T.-K. Lau, X. Lu, C. Zhu, H. Peng, P. A. Johnson, *Joule* **2019**, *3*, 1140–1151.
- [6] B. Fan, D. Zhang, M. Li, W. Zhong, Z. Zeng, L. Ying, F. Huang, Y. Cao, Sci. China Chem. 2019, 62, 746–752.
- [7] S. Lucas, T. Leydecker, P. Samorì, E. M. Osteritz, P. Baeuerle, n.d., DOI 10.26434/chemrxiv.9892067.
- [8] G. Feng, J. Li, Y. He, W. Zheng, J. Wang, C. Li, Z. Tang, A. Osvet, N. Li, C. J. Brabec, Joule 2019, 3, 1765–1781.
- [9] C. Li, Y. Lin, F. Li, L. Zhu, D. Sun, L. Shen, Y. Chen, S. Ruan, RSC Adv. 2015, 5, 80561–80567.
- [10] A. Bhirud, S. Sathaye, R. Waichal, C.-J. Park, B. Kale, J. Mater. Chem. A 2015, 3, 17050–17063.
- **2015**, *3*, 17050–17063. [11] H. Köse, Ş. Karaal, A. O. Aydın, H. Akbulut, *J. Power Sources* **2015**, *295*,
- 235–245.[12] L. Fang, K. Huang, B. Zhang, B. Liu, Y. Liu, Q. Zhang, RSC Adv. 2014, 4, 48986–48993.
- [13] W. J. E. Beek, M. M. Wienk, R. a. J. Janssen, *Adv. Mater.* **2004**, *16*, 1009–
- [14] Z. Liang, R. Gao, J.-L. Lan, O. Wiranwetchayan, Q. Zhang, C. Li, G. Cao, Sol. Energy Mater. Sol. Cells 2013, 117, 34–40.
- [15] A. S. Shaporev, V. K. Ivanov, A. E. Baranchikov, O. S. Polezhaeva, Y. D. Tret'yakov, Russ. J. Inorg. Chem. 2007, 52, 1811–1816.

- [16] Y. Huang, P. Cai, P. Ren, X. Zhang, Y. Du, Z. Zou, J. Xiong, X. Xue, J. Zhang, J. Chen, *Phys. Status Solidi A* n.d., 0, DOI 10.1002/pssa.201800113.
- [17] P. Rai, Y.-T. Yu, Sens. Actuators B 2012, 173, 58-65.
- [18] H. Zhu, C.-X. Shan, B. Yao, B.-H. Li, J.-Y. Zhang, Z.-Z. Zhang, D.-X. Zhao, D.-Z. Shen, X.-W. Fan, Y.-M. Lu, Adv. Mater. 2009, 21, 1613–1617.
- [19] H. W. Kroto, J. R. Heath, S. C. O'Brien, R. F. Curl, R. E. Smalley, *Nature* 1985, 318, 162–163.
- [20] T. Akasaka, Angew. Chem. Int. Ed. n.d., 47, 633-633.
- [21] S. F. A. Acquah, A. V. Penkova, D. A. Markelov, A. S. Semisalova, B. E. Leonhardt, J. M. Magi, ECS J. Solid State Sci. Technol. 2017, 6, M3155– M3162.
- [22] B. C. Yadav, R. Kumar, 2008.
- [23] R. Bacon, J. Appl. Phys. 1960, 31, 283-290.
- [24] D. Brus, O. Mykhailiv, L. Echegoyen, M. Plonska-Brzezinska, in *Carbon Nanomater. Sourceb.*, CRC Press, **2016**, pp. 275–302.
- [25] M. E. Plonska-Brzezinska, M. Lewandowski, M. Błaszyk, A. Molina-Ontoria, T. Luciński, L. Echegoyen, ChemPhysChem 2012, 13, 4134–4141.
- [26] V. L. Kuznetsov, A. L. Chuvilin, Y. V. Butenko, I. Yu. Mal'kov, V. M. Titov, Chem. Phys. Lett. 1994, 222, 343–348.
- [27] A. Palkar, F. Melin, C. M. Cardona, B. Elliott, A. K. Naskar, D. D. Edie, A. Kumbhar, L. Echegoyen, Chem. Asian J. 2007, 2, 625–633.
- [28] V. L. Kuznetsov, A. L. Chuvilin, E. M. Moroz, V. N. Kolomiichuk, Sh. K. Shaikhutdinov, Yu. V. Butenko, I. Yu. Mal'kov, Carbon 1994, 32, 873–882.
- [29] D. M. Bobrowska, K. Brzezinski, L. Echegoyen, M. E. Plonska-Brzezinska, Fuller. Nanotub. Carbon Nanostructures 2017, 00–00.
- [30] A. N. Papathanassiou, O. Mykhailiv, L. Echegoyen, I. Sakellis, M. E. Plonska-Brzezinska, J. Phys. Appl. Phys. 2016, 49, 285305.
- [31] A. N. Papathanassiou, M. E. Plonska-Brzezinska, O. Mykhailiv, L. Echegoyen. I. Sakellis. Synth. Met. 2015, 209, 583–587.
- [32] O. Mykhailiv, M. Imierska, M. Petelczyc, L. Echegoyen, M. E. Plonska-Brzezinska, Chem. Eur. J. 2015, 21, 5783–5793.
- [33] M. E. Plonska-Brzezinska, D. M. Brus, A. Molina-Ontoria, L. Echegoyen, RSC Adv. 2013, 3, 25891.
- [34] K. K. Kim, D. Kim, S. K. Kim, S. M. Park, J. K. Song, Chem. Phys. Lett. 2011, 511, 116–120.
- [35] H. Zhang, D. Yang, Y. Ji, X. Ma, J. Xu, D. Que, J. Phys. Chem. B 2004, 108, 3955–3958.
- [36] B. Liu, H. C. Zeng, J. Am. Chem. Soc. 2003, 125, 4430-4431.
- [37] W. Yu, X. Li, X. Gao, Cryst. Growth Des. **2005**, *5*, 151–155.
- [38] S.-Y. Chu, T.-M. Yan, S.-L. Chen, J. Mater. Sci. Lett. 2000, 19, 349–352.
- [39] C. L. Carnes, K. J. Klabunde, Langmuir 2000, 16, 3764-3772.
- [40] M. Wang, Y. Zhou, Y. Zhang, S. H. Hahn, E. J. Kim, CrystEngComm 2011, 13, 6024.
- [41] R. A. McBride, J. M. Kelly, D. E. McCormack, J. Mater. Chem. 2003, 13, 1196–1201.
- [42] A. Top, H. Çetinkaya, Mater. Chem. Phys. 2015, 167, 77–87.
- [43] S. Yamabi, H. Imai, J. Mater. Chem. 2002, 12, 3773–3778.
- [44] R. M. A. Lieth, *Preparation and Crystal Growth of Materials with Layered Structures*, Springer Science & Business Media, **2013**.
- [45] A. E. Aleksenskii, M. V. Baidakova, A. Ya. Vul', V. Yu. Davydov, Yu. A. Pevtsova, Phys. Solid State 1997, 39, 1007–1015.
- [46] S. Tomita, A. Burian, J. C. Dore, D. LeBolloch, M. Fujii, S. Hayashi, *Carbon* 2002, 40, 1469–1474.
- [47] J. S. Suroshe, S. S. Garje, J. Mater. Chem. A 2015, 3, 15650-15660.
- [48] S. S. Kumar, P. Venkateswarlu, V. R. Rao, G. N. Rao, Int. Nano Lett. 2013, 3, 30.
- [49] D. Ramimoghadam, M. Hussein, Y. Taufiq-Yap, Int. J. Mol. Sci. 2012, 13, 13275–13293.
- [50] A. Moezzi, M. Cortie, A. McDonagh, Dalton Trans. 2011, 40, 4871-4878.
- [51] S. Sepulveda-Guzman, B. Reeja-Jayan, E. de la Rosa, A. Torres-Castro, V. Gonzalez-Gonzalez, M. Jose-Yacaman, *Mater. Chem. Phys.* 2009, 115, 172–178.
- [52] A. C. Ferrari, J. Robertson, *Phys. Rev. B* **2000**, *61*, 14095–14107.
- [53] E. D. Obraztsova, M. Fujii, S. Hayashi, V. L. Kuznetsov, Yu. V. Butenko, A. L. Chuvilin, Carbon 1998, 36, 821–826.
- [54] D. Roy, M. Chhowalla, H. Wang, N. Sano, I. Alexandrou, T. W. Clyne, G. A. J. Amaratunga, Chem. Phys. Lett. 2003, 373, 52–56.
- [55] S. K. Mohanta, D. C. Kim, H. K. Cho, S. J. Chua, S. Tripathy, J. Cryst. Growth 2008, 310, 3208–3213.
- [56] R. Zhang, P.-G. Yin, N. Wang, L. Guo, Solid State Sci. 2009, 11, 865-869.
- [57] S. B. Yahia, L. Znaidi, A. Kanaev, J. P. Petitet, Spectrochim. Acta Part A 2008, 71, 1234–1238.
- [58] R. P. Wang, G. Xu, P. Jin, Phys. Rev. B 2004, 69, DOI 10.1103/ PhysRevB.69.113303.





- [59] G. H. G. Ahmed, R. B. Laíño, J. A. G. Calzón, M. E. D. García, Beilstein J. Nanotechnol. 2016, 7, 758-766.
- [60] S. Y. Sawant, R. S. Somani, A. B. Panda, H. C. Bajaj, Mater. Lett. 2013, 94, 132-135.
- [61] M. E. Plonska-Brzezinska, A. T. Dubis, A. Lapinski, A. Villalta-Cerdas, L. Echegoyen, ChemPhysChem 2011, 12, 2659-2668.
- [62] K. Bharathi Yazhini, H. Gurumallesh Prabu, RSC Adv. 2015, 5, 49062-
- [63] M. S. White, D. C. Olson, S. E. Shaheen, N. Kopidakis, D. S. Ginley, Appl. Phys. Lett. 2006, 89, 143517.
- [64] D. C. Olson, J. Piris, R. T. Collins, S. E. Shaheen, D. S. Ginley, Thin Solid Films 2006, 496, 26-29.
- [65] H. Mizuno, K. Nagano, S. Tomita, H. Yanagi, I. Hiromitsu, Thin Solid Films 2018, 654, 69-76.

- [66] M. E. Plonska-Brzezinska, J. Mazurczyk, B. Palys, J. Breczko, A. Lapinski, A. T. Dubis, L. Echegoyen, Chem. Eur. J. 2012, 18, 2600-2608.
- [67] D. M. Bobrowska, J. Czyrko, K. Brzezinski, L. Echegoyen, M. E. Plonska-Brzezinska, Fuller. Nanotub. Carbon Nanostructures 2017, 25, 185–192.

Manuscript received: September 18, 2019 Revised manuscript received: October 27, 2019 Accepted manuscript online: November 24, 2019 Version of record online: December 5, 2019

www.chemnanomat.org